RSC Advances

ROYAL SOCIETY OF CHEMISTRY

PAPER

View Article Online
View Journal | View Issue

Cite this: *RSC Adv.*, 2026, **16**, 7011

High-temperature physical properties of tungsten: implications for near-field thermophotovoltaic energy conversion

Tran Dinh Cuong *[a] and Anh D. Phan [bc]

Tungsten plays a crucial role in the development of near-field thermophotovoltaic devices. However, available information about tungsten is insufficient to model radiative heat transfer at elevated temperatures. In this study, we develop a statistical theory to evaluate finite-temperature effects on the physical properties of tungsten up to 2000 K, corresponding to extreme conditions in practical emitters. First, the moment expansion technique is applied to calculate the atomic volume, the mechanical modulus, and the Debye temperature. Quasi-harmonic and anharmonic contributions are clarified *via* simple analytical formulas for free energies. Then, we utilize these thermodynamic quantities to deduce the electrical resistivity from the Bloch–Grüneisen law and the dielectric function from the Drude–Lorentz model. Our calculations are in good agreement with previous experiments. Finally, based on fluctuational electrodynamics, we reconsider energy-conversion processes in a representative system made of tungsten and GaSb. Both radiative and electric power densities will be severely underestimated if the thermal variation of input parameters is ignored. This result suggests that experimental and computational databases need to be expanded from low to high temperatures before actualizing the potential applications of near-field thermophotovoltaics.

Received 28th December 2025
Accepted 23rd January 2026

DOI: 10.1039/d5ra10049f

rsc.li/rsc-advances

1 Introduction

In recent years, "thermophotovoltaic" (TPV) has become an attractive keyword in the field of energy conversion.[1–3] This modern technology utilizes photovoltaic cells to transform thermal radiation from selective emitters into electric power for human activities. The transformation does not cause noise pollution because there is no moving part in solid-state TPV systems. Besides, various heat sources can be exploited to increase emitter temperatures, including solar irradiation, fuel combustion, radioactive decay, and industrial waste heat. In particular, the TPV efficiency can be up to 40%,[4] which is hard to achieve using conventional steam turbines. These outstanding advantages have opened a flexible, economical, and eco-friendly avenue for addressing global energy problems.

To generate more electricity from TPV devices, physicists have paid meticulous attention to radiative heat transfers in the near-field (NF) regime.[5–7] When the vacuum gap between the selective emitter and the photovoltaic cell is shorter than the Wien characteristic wavelength, both propagating and evanescent waves can directly contribute to the flow of radiative energy. This fascinating phenomenon originates from quantum tunneling effects, which enable evanescent fields to penetrate inside TPV materials rather than undergoing exponential decays in the vacuum. The appearance of evanescent modes can break down the blackbody (Planckian) limit of thermal radiation, thereby boosting the production of electric power by orders of magnitude.[8] Hence, NF TPV systems have an enormous potential to compete with thermionic and thermoelectric generators in the energy conversion race.

To realize NF TPV applications, the physical community needs to find an appropriate emitter material. Among prospective candidates, tungsten has attracted close interest due to its splendid thermal stability, spectral emissivity, and material compatibility.[9–11] This refractory metal has been widely used to develop NF TPV converters with the aid of fluctuational electrodynamics (FED).[8] It has been predicted that the power output density would reach 10^5 to 10^6 W m^{-2} at a 10 nm distance.[7] Nevertheless, since the dielectric functions of tungsten have not been fully understood at elevated temperatures, FED calculations have been primarily performed with experimental data at $T_r = 300$ K.[12–14] This is a crucial problem because practical emitters operate in intensely hot environments.[5–7] Their working temperature can be up to 2000 K, which is sufficiently high to cause dramatic changes in physical quantities. Thus, the assumption of insensitive optical properties significantly increases the uncertainty of FED-based theoretical predictions.

[a]*Phenikaa Institute for Advanced Study, Phenikaa University, Yen Nghia, Ha Dong, Hanoi 12116, Vietnam. E-mail: cuong.trandinh@phenikaa-uni.edu.vn*

[b]*Center for Materials Innovation and Technology, VinUniversity, Hanoi 100000, Vietnam*

[c]*College of Engineering and Computer Sciences, VinUniversity, Hanoi 100000, Vietnam*

Many attempts have been made to consider finite-temperature effects. Minissale *et al.*[15] incorporated a high-power laser into their spectroscopic system to carry out reflectivity measurements between 300 and 925 K. On that basis, they developed the Drude–Lorentz formalism to predict the optical behaviors of tungsten during isobaric heating. Shortly thereafter, Xu *et al.*[16] combined ellipsometry experiments with *ab initio* computations to elucidate the underlying physics of inter- and intra-band dielectric functions from 100 to 900 K. Their experimental and computational results advanced our understanding of electron–electron and electron–phonon interactions in transition metals, including chromium, molybdenum, and tungsten. To augment optical databases, Arya *et al.*[17] extended the experimentally accessible region to 1273 K. The influences of sample thickness, grain boundary, and surface scattering were also carefully discussed. However, a long extrapolation is still required to reach the emitter temperature of 2000 K in NF TPV devices. In addition, a strong consensus about the Drude–Lorentz parameters remains unestablished. While the plasma frequency spans from 5.2 to 7.8 eV at ambient pressure and temperature, the collision frequency spans from 0.014 to 0.064 eV under the same conditions.[15–17] Therefore, alternative strategies are needed to determine the high-temperature physical properties of tungsten.

Here, we introduce a potential alternative based on a combination of basic theories in solid-state physics. Our inspiration comes from the intimate connection between thermodynamic, elastic, electrical, and optical quantities in metallic crystals. This is clearly reflected in the Anderson equation,[18] the Bloch–Grüneisen law,[19] and the Drude–Lorentz model.[20] We also employ the statistical moment method (SMM) to incorporate quasi-harmonic and anharmonic effects into theoretical calculations.[21–23] SMM results are entered into FED formulas[24] to reassess the energy transformation between tungsten and GaSb parallel plates at the nanoscale. GaSb is chosen for constructing the photovoltaic cell because of its high absorption coefficient, strong radiation resistance, and excellent spectral responsiveness.[25] Our approximations are thoroughly compared with practical measurements to draw a more comprehensive physical picture of tungsten in severe environments. We hope our study can suggest more efficient and effective ways to model TPV systems in the NF regime.

2 Method

2.1 Core ideas

Let us concretize our strategy (see Fig. 1). It has been demonstrated that tungsten could retain its bcc lattice over an extensive range of temperatures (T) and pressures (P).[26] This unique monomorphism enables us to rapidly determine the total free energy F using the SMM theory,[21] which is well-suited to handle vibrational excitations in symmetric structures. Having the analytical expression of F at hand, we can easily deduce the atomic volume V of tungsten from the equation of state. Simultaneously, it is possible to infer bulk (B) and shear (G) moduli from the modified cylindrical method.[23] Inserting B and G into the Anderson equation[18] provides us with the Debye temperature θ_D—a critical thermodynamic parameter in the field of condensed matter physics. One of the most appealing aspects of θ_D is the ability to calculate the electrical resistivity ρ *via* the Bloch–Grüneisen law.[19] We can evaluate the relative importance of electron–electron *versus* electron-phonon scatterings under various thermodynamic conditions. Details about V and ρ help us capture the temperature dependence of the plasma frequency Ω_p and the collision frequency Γ_D.[27] In other words, the dielectric function ε during isobaric heating can be immediately derived from the Drude–Lorentz model.[20] Combining these results with FED formulas[24] leads to radiative (P_{rad}) and electric (P_{el}) power densities in the NF TPV converter made of tungsten and GaSb.

The above analyses reveal how to connect different physical properties within a simple theoretical framework. There are two key advantages we would like to emphasize here. First, apart from the energy conversion, our approach can also predict the volumetric expansion and the mechanical deformation of emitter materials. These predictions would contribute to enhancing the safety, longevity, and efficiency of NF TPV devices. Second, equation-of-state databases are much larger than optical ones due to the rapid development of *ab initio*, shock-wave, ramp-wave, and diamond-anvil-cell techniques.[28–30] Information about the atomic volume, the elastic modulus, and the Debye temperature is available for numerous crystals over a wide range of P–T values. Hence, we can leverage these abundant resources to determine FED inputs, accelerate computational processes, remove pressure-temperature barriers, and search for prospective NF TPV candidates.

2.2 Tungsten properties

After clarifying core ideas, let us formulate key equations for tungsten. Its total free energy F can be decomposed into ground-state (F_0), quasi-harmonic (F_{qh}), and anharmonic (F_{ah}) parts by employing the Born–Oppenheimer approximation as[21–23]

$$F = F_0 + F_{qh} + F_{ah}. \quad (1)$$

Here, we neglect the explicit contributions of electrons and vacancies to the Helmholtz free energy because the maximum temperature we consider is 2000 K, corresponding to NF TPV applications.[5–7] Recent *ab initio* calculations[31] have shown that electronic excitations could not significantly alter the isobaric heat capacity, the linear expansion coefficient, and the adiabatic bulk modulus of tungsten in our studied temperature range. Besides, since the equilibrium concentration of lattice vacancies is less than 5×10^{-8},[32] we can apply the perfect bcc model to construct the free-energy surface.[23] This model allows us to perform SMM analyses with the pairwise interatomic potential $\varphi(r)$, where r is the nearest neighbor distance. Similar to previous studies,[33–35] we chose the Mie–Lennard-Jones interaction function because of its mathematical simplicity,

$$F_0 = 4\varphi = \frac{4D}{b-a}\left[a\left(\frac{r_0}{r}\right)^b - b\left(\frac{r_0}{r}\right)^a\right]. \quad (2)$$

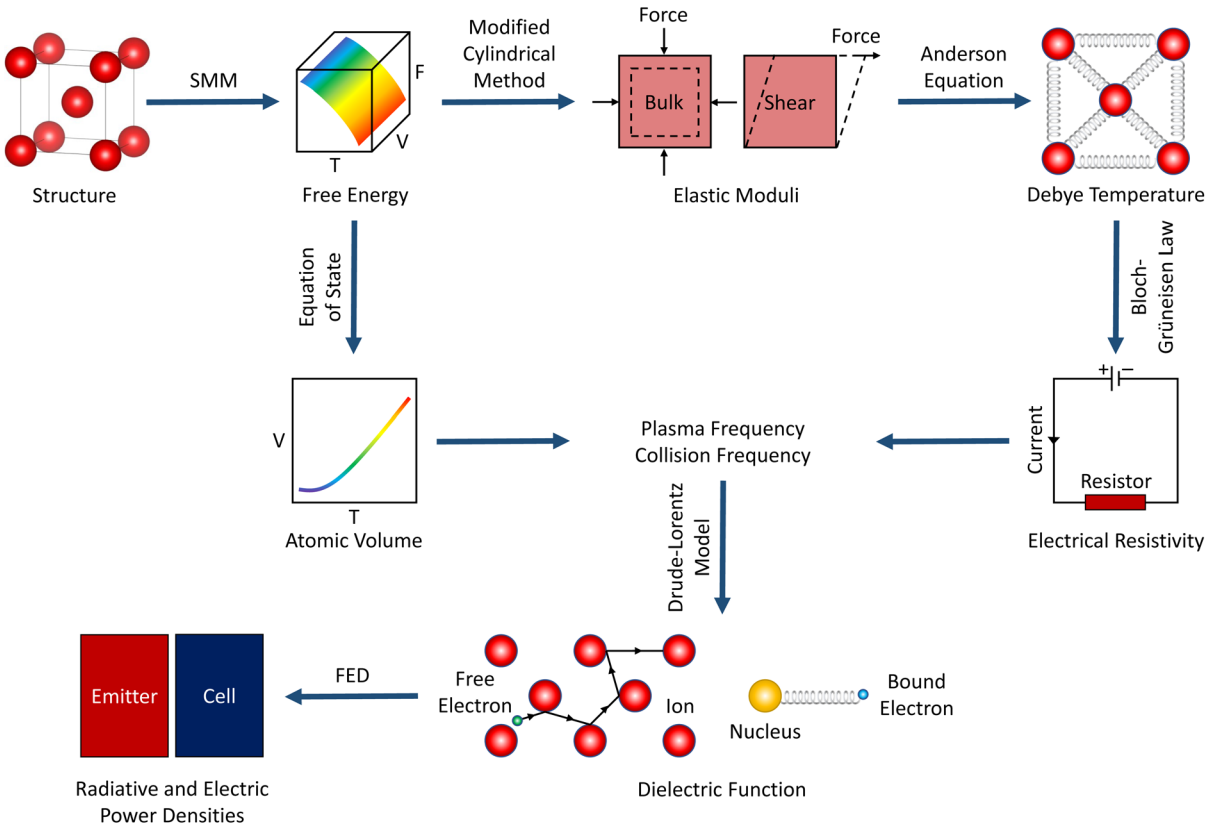

Fig. 1 (Color online) Schematic description of our theoretical approach.

The potential parameters of tungsten are $D = 2.2067$ eV, $r_0 = 2.7365$ Å, $a = 4.06$, and $b = 8.58$.[36] The accuracy of eqn (2) will be validated in Section 3.

The Mie–Lennard-Jones potential works quite well within the first coordination shell.[36] Thus, we can employ the Leibfried–Ludwig theory[37] to extract the coupling parameters of tungsten (k, γ_1, and γ_2) from its ground-state free energy as

$$k = \left(\frac{\partial^2 F_0}{\partial u_\zeta^2}\right)_{\mathrm{eq}} = \frac{4}{3}\frac{\mathrm{d}^2\varphi}{\mathrm{d}r^2} + \frac{8}{3r}\frac{\mathrm{d}\varphi}{\mathrm{d}r} = m\omega_E^2,$$
$$\gamma_1 = \frac{1}{24}\left(\frac{\partial^4 F_0}{\partial u_\zeta^4}\right)_{\mathrm{eq}} = \frac{1}{54}\frac{\mathrm{d}^4\varphi}{\mathrm{d}r^4} + \frac{2}{9r}\frac{\mathrm{d}^3\varphi}{\mathrm{d}r^3} - \frac{2}{9r^2}\frac{\mathrm{d}^2\varphi}{\mathrm{d}r^2} + \frac{2}{9r^3}\frac{\mathrm{d}\varphi}{\mathrm{d}r} \quad (3)$$
$$\gamma_2 = \frac{1}{4}\left(\frac{\partial^4 F_0}{\partial u_\zeta^2 \partial u_\eta^2}\right)_{\mathrm{eq}} = \frac{1}{9}\frac{\mathrm{d}^4\varphi}{\mathrm{d}r^4} + \frac{2}{3r^2}\frac{\mathrm{d}^2\varphi}{\mathrm{d}r^2} - \frac{2}{3r^3}\frac{\mathrm{d}\varphi}{\mathrm{d}r},$$

where m is the atomic mass, ω_{E} is the vibrational frequency, and u_ζ is the ζ projection of the ionic displacement vector ($\zeta \neq \eta = x, y, z$). Eqn (3) is very useful for evaluating quasi-harmonic and anharmonic contributions. Specifically, F_{qh} is given by[21–23]

$$F_{\mathrm{qh}} = \frac{3}{2}\hbar\omega_{\mathrm{E}} + 3k_{\mathrm{B}}T\ \ln\left[1 - \exp\left(-\frac{\hbar\omega_{\mathrm{E}}}{k_{\mathrm{B}}T}\right)\right], \quad (4)$$

where $\hbar$ and k_{B} are fundamental physical constants. While the first term originates from the zero-point motion, the second term stems from the thermal vibration. Eqn (4) reminds us of the Einstein crystal in quantum mechanics—a simple but effective approximation for investigating high-temperature properties.[29] In addition, F_{ah} is quantified by the thermodynamic integration technique,[38]

$$F_{\mathrm{ah}} = 3\int_0^{\gamma_1}\langle u_\zeta^4\rangle \mathrm{d}\gamma_1 + 3\int_0^{\gamma_2}\langle u_\zeta^2\rangle\langle u_\eta^2\rangle \mathrm{d}\gamma_2, \quad (5)$$

where angle brackets stand for average values in the equilibrium state. It is feasible to utilize the density matrix to establish the SMM recurrence relation among ionic displacement moments.[21] This strategy helps us deduce $\langle u_\zeta^4\rangle$ and $\langle u_\zeta^2\rangle$ from $\langle u_\zeta\rangle$—a well-determined quantity in the force-balance criterion.[33–35] Note that we do not consider the influence of sixth- or higher-order anharmonic terms because their absence does not reduce the quality of free-energy calculations, as demonstrated in the case of tantalum.[23] The above arguments lead to[22]

$$F_{\mathrm{ah}} = \frac{{k_{\mathrm{B}}}^2T^2}{k^2}\left[3\gamma_2X^2 - \gamma_1(X+2)\right] + \frac{2{k_{\mathrm{B}}}^3T^3}{k^4}(X+2)\left[2{\gamma_2}^2X - 3\gamma_1(\gamma_1+2\gamma_2)(X+1)\right], \quad (6)$$

where $X = \frac{\hbar\omega_{\mathrm{E}}}{2k_{\mathrm{B}}T}\coth\frac{\hbar\omega_{\mathrm{E}}}{2k_{\mathrm{B}}T}$ plays a role in distinguishing quantum ($X \to \infty$) and classical ($X \to 1$) domains.

Having calculated the total free energy of tungsten, we can determine the atomic volume by solving the equation of state,[38]

$$P = -\left(\frac{\partial F}{\partial V}\right)_T. \quad (7)$$

The left-hand side of eqn (7) is set to 0 GPa, relevant to the working pressure of NF TPV devices.[5–7] Details about *P–V–T* correlations are leveraged to derive the isothermal compressibility χ_T, the volumetric expansivity β_P, and the isochoric heat capacity C_V.[38] These thermodynamic properties are valuable for studying the bulk deformation of tungsten under adiabatic conditions,[38]

$$B = \frac{1}{\chi_T}\left(1 + \frac{{\beta_P}^2 V}{\chi_T C_V} T\right). \tag{8}$$

Moreover, it is possible to compute the Young modulus E of tungsten *via* the modified cylindrical method.[23] Based on the room-temperature Poisson ratio of 0.293,[39] we have

$$E = \frac{17k}{10\pi r}\left[1 + \frac{16{k_B}^2 T^2}{k^4}(\gamma_1 + \gamma_2)^2 (X+1)(X+2)\right]^{-1}. \tag{9}$$

Entering eqn (8) and (9) into the classical theory of elasticity gives us the shear modulus of tungsten as[38]

$$G = \frac{3BE}{9B - E}. \tag{10}$$

The mechanical quantities above are linked with the Debye temperature *via* the Anderson equation,[18]

$$\theta_D = \frac{2\pi\hbar}{k_B}\left(\frac{3}{4\pi V}\right)^{\frac{1}{3}}\left[\frac{2}{3}\left(\frac{GV}{m}\right)^{-\frac{3}{2}} + \frac{1}{3}\left(\frac{3B+4G}{3m}V\right)^{-\frac{3}{2}}\right]^{-\frac{1}{3}}. \tag{11}$$

Intimate knowledge of Debye solids can open up promising avenues for modeling electrical properties *via* thermoelastic data. Specifically, we separate the total resistivity of tungsten into three additive components using the Matthiessen rule,[40]

$$\rho = \rho_0 + \rho_{e-e} + \rho_{p-e}. \tag{12}$$

The residual resistivity ρ_0 originates from structural imperfections during material processing and remains unchanged along the ambient isobar. Meanwhile, the intrinsic resistivities ρ_{e-e} and ρ_{p-e} are temperature-dependent because they arise from electron–electron and phonon–electron scatterings. Applying the Bloch–Grüneisen law[19] yields

$$\begin{aligned}\rho_{e-e} &= C_{e-e}\frac{T^2}{{\theta_D}^3}\int_0^{\frac{\theta_D}{T}}\frac{t^2 \mathrm{d}t}{(\mathrm{e}^t - 1)(1 - \mathrm{e}^{-t})},\\ \rho_{p-e} &= C_{p-e}\frac{T^5}{{\theta_D}^6}\int_0^{\frac{\theta_D}{T}}\frac{t^5 \mathrm{d}t}{(\mathrm{e}^t - 1)(1 - \mathrm{e}^{-t})},\end{aligned} \tag{13}$$

where C_{e-e} and C_{p-e} are metal-specific constants. In the low-temperature limit, eqn (13) enables us to rewrite eqn (12) with

$$\rho = \rho_0 + 3.2899 C_{e-e}\frac{T^2}{{\theta_D}^3} + 124.4313 C_{p-e}\frac{T^5}{{\theta_D}^6}. \tag{14}$$

Fitting eqn (14) with experimental data[41] at $1 \le T \le 40$ K provides $\rho_0 = 0.000015$ μΩ cm, $C_{e-e} = 12.4459$ μΩ cm K, and $C_{p-e} = 14298.4974$ μΩ cm K. From there, we can clarify the thermal variation of plasma and collision frequencies by[27]

$$\begin{aligned}\Delta\Omega_p &= \Omega_p(T) - \Omega_p(T_r) = \Omega_p(T_r)\left[\sqrt{\frac{V(T_r)}{V(T)}} - 1\right],\\ \Delta\Gamma_D &= \Gamma_D(T) - \Gamma_D(T_r) = \Gamma_D(T_r)\left[\frac{V(T_r)}{V(T)}\frac{\rho(T)}{\rho(T_r)} - 1\right].\end{aligned} \tag{15}$$

The dielectric function of tungsten is then determined by the Drude–Lorentz model as[20]

$$\begin{aligned}\varepsilon &= \varepsilon_D + \varepsilon_L,\\ \varepsilon_D &= 1 - \frac{{\Omega_p}^2}{\omega(\omega + i\Gamma_D)},\\ \varepsilon_L &= \sum_{j=1}^{4}\frac{f_j {\Omega_p}^2}{f_0\left({\omega_j}^2 - \omega^2 - i\omega\Gamma_j\right)},\end{aligned} \tag{16}$$

where ω is the angular frequency, i is the imaginary unit, ε_D represents the contribution of free electrons, and ε_L characterizes the contribution of bound electrons. Semi-empirical parameters f_0, f_j, ω_j, and Γ_j are listed in Table 1.[42] Their temperature dependence can be safely ignored, as suggested by the latest ellipsometry measurements of Arya *et al.*[17] on tungsten thin films and bulk substrates from 300 to 1273 K.

Table 1 The Drude–Lorentz parameters of tungsten measured at room temperature ($T_r = 300$ K)[42]

Parameter	Value	Unit
$\hbar\Omega_p$	6.000	eV
$\hbar\Gamma_D$	0.064	eV
f_0	0.206	None
f_1	0.054	None
$\hbar\omega_1$	1.004	eV
$\hbar\Gamma_1$	0.530	eV
f_2	0.166	None
$\hbar\omega_2$	1.917	eV
$\hbar\Gamma_2$	1.281	eV
f_3	0.706	None
$\hbar\omega_3$	3.580	eV
$\hbar\Gamma_3$	3.332	eV
f_4	2.590	None
$\hbar\omega_4$	7.498	eV
$\hbar\Gamma_4$	5.836	eV

2.3 Fluctuational electrodynamics

Eqn (15) and (16) are advantageous for shedding light on the conversion of heat into electricity in harsh environments. To be more specific, we consider the electromagnetic interaction between the hot tungsten emitter (ε, T) and the cool GaSb cell (ε_r, T_r) at the nanoscale, where the relative permittivity ε_r of the semiconductor is taken from the empirical method of Adachi[43] and the Python script of Polyanskiy.[44] Our NF TPV system is built from two semi-infinite parallel plates separated by a vacuum space of thickness d (see Fig. 2). This geometric configuration is conceptually important because it provides direct insights into the role of quantum-mechanical and finite-

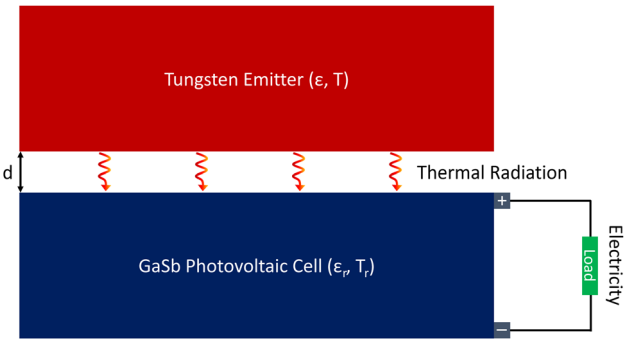

Fig. 2 (Color online) Illustration of our NF TPV converter. The plate–plate configuration is selected due to its simplicity and popularity. FED formulas for radiative heat transfers between two closely spaced parallel plates have been thoroughly developed and validated. The GaSb cell is responsible for transforming thermal radiation from the tungsten emitter into electricity through photovoltaic effects.

temperature effects through well-established FED formulas.[6–8] In the FED framework, the sources of thermal radiation are randomly activated electric currents inside solid objects. Although the statistical average of these random currents vanishes, their correlations are quantitatively determined by the fluctuation-dissipation theorem.[45,46] Solving the Maxwell equations[20] with the aid of FED approximations yields[24]

$$P_{\mathrm{rad}} = \int_0^\infty \frac{d\omega}{4\pi^2}\left[\frac{\hbar\omega}{\exp\left(\frac{\hbar\omega}{k_{\mathrm{B}}T}\right)-1} - \frac{\hbar\omega}{\exp\left(\frac{\hbar\omega}{k_{\mathrm{B}}T_{\mathrm{r}}}\right)-1}\right] \times \int_0^\infty d\kappa\kappa\left[\tau_{\mathrm{s}}(\omega,\kappa,d)+\tau_{\mathrm{p}}(\omega,\kappa,d)\right], \tag{17}$$

where κ is the wavevector component parallel to the emitter and cell surfaces. If we know the Fresnel coefficients r_1^{s}, r_2^{s}, r_1^{p}, and r_2^{p}, we can explicitly express the transmission probabilities τ_{s} and τ_{p} for s- and p-polarized modes as[24]

$$\tau_{\mathrm{s}} = \begin{cases} \dfrac{\left(1-|r_1^{\mathrm{s}}|^2\right)\left(1-|r_2^{\mathrm{s}}|^2\right)}{\left|1-r_1^{\mathrm{s}}r_2^{\mathrm{s}}\exp\left(2i\sqrt{\kappa_0^2-\kappa^2}\right)\right|^2}, & \kappa<\kappa_0, \\ \dfrac{4\mathrm{Im}(r_1^{\mathrm{s}})\mathrm{Im}(r_2^{\mathrm{s}})\exp\left[-2d\mathrm{Im}\left(\sqrt{\kappa_0^2-\kappa^2}\right)\right]}{\left|1-r_1^{\mathrm{s}}r_2^{\mathrm{s}}\exp\left(2i\sqrt{\kappa_0^2-\kappa^2}\right)\right|^2}, & \kappa>\kappa_0, \end{cases}$$

$$\tau_{\mathrm{p}} = \begin{cases} \dfrac{\left(1-|r_1^{\mathrm{p}}|^2\right)\left(1-|r_2^{\mathrm{p}}|^2\right)}{\left|1-r_1^{\mathrm{p}}r_2^{\mathrm{p}}\exp\left(2i\sqrt{\kappa_0^2-\kappa^2}\right)\right|^2}, & \kappa<\kappa_0, \\ \dfrac{4\mathrm{Im}(r_1^{\mathrm{p}})\mathrm{Im}(r_2^{\mathrm{p}})\exp\left[-2d\mathrm{Im}\left(\sqrt{\kappa_0^2-\kappa^2}\right)\right]}{\left|1-r_1^{\mathrm{p}}r_2^{\mathrm{p}}\exp\left(2i\sqrt{\kappa_0^2-\kappa^2}\right)\right|^2}, & \kappa>\kappa_0, \end{cases} \tag{18}$$

where κ_0 is the wavenumber in vacuum. Eqn (18) captures the underlying physics of both propagating photons ($\kappa < \kappa_0$) and evanescent ones ($\kappa > \kappa_0$). Its inputs are calculated by[24]

$$\begin{aligned} r_1^{\mathrm{s}} &= \frac{\sqrt{\kappa_0^2-\kappa^2}-\sqrt{\varepsilon\kappa_0^2-\kappa^2}}{\sqrt{\kappa_0^2-\kappa^2}+\sqrt{\varepsilon\kappa_0^2-\kappa^2}}, \\ r_2^{\mathrm{s}} &= \frac{\sqrt{\kappa_0^2-\kappa^2}-\sqrt{\varepsilon_{\mathrm{r}}\kappa_0^2-\kappa^2}}{\sqrt{\kappa_0^2-\kappa^2}+\sqrt{\varepsilon_{\mathrm{r}}\kappa_0^2-\kappa^2}}, \\ r_1^{\mathrm{p}} &= \frac{\varepsilon\sqrt{\kappa_0^2-\kappa^2}-\sqrt{\varepsilon\kappa_0^2-\kappa^2}}{\varepsilon\sqrt{\kappa_0^2-\kappa^2}+\sqrt{\varepsilon\kappa_0^2-\kappa^2}}, \\ r_2^{\mathrm{p}} &= \frac{\varepsilon_{\mathrm{r}}\sqrt{\kappa_0^2-\kappa^2}-\sqrt{\varepsilon_{\mathrm{r}}\kappa_0^2-\kappa^2}}{\varepsilon_{\mathrm{r}}\sqrt{\kappa_0^2-\kappa^2}+\sqrt{\varepsilon_{\mathrm{r}}\kappa_0^2-\kappa^2}}. \end{aligned} \tag{19}$$

Assuming that each photon absorbed by GaSb excites an electron–hole pair, the photogeneration current I_{ph} is estimated by[5]

$$I_{\mathrm{ph}} = e\int_{\frac{E_{\mathrm{g}}}{\hbar}}^\infty \frac{d\omega}{4\pi^2}\left[\frac{1}{\exp\left(\frac{\hbar\omega}{k_{\mathrm{B}}T}\right)-1} - \frac{1}{\exp\left(\frac{\hbar\omega}{k_{\mathrm{B}}T_{\mathrm{r}}}\right)-1}\right] \times \int_0^\infty d\kappa\kappa\left[\tau_{\mathrm{s}}(\omega,\kappa,d)+\tau_{\mathrm{p}}(\omega,\kappa,d)\right], \tag{20}$$

where $e = 1.6022 \times 10^{-19}$ C is the elementary charge, and $E_{\mathrm{g}} = 0.7$ eV is the band-gap energy. Eqn (20) allows us to infer the open-circuit voltage V_{oc} and the fill factor FF from[5]

$$\begin{aligned} V_{\mathrm{oc}} &= \frac{k_{\mathrm{B}}T_{\mathrm{r}}}{\mathrm{e}}\ln\left(\frac{I_{\mathrm{ph}}}{I_0}\right), \\ \mathrm{FF} &= \left[1-\frac{1}{\ln\left(\frac{I_{\mathrm{ph}}}{I_0}\right)}\right]\left\{1-\frac{\ln\left[\ln\left(\frac{I_{\mathrm{ph}}}{I_0}\right)\right]}{\ln\left(\frac{I_{\mathrm{ph}}}{I_0}\right)}\right\}, \end{aligned} \tag{21}$$

where $I_0 = 6 \times 10^{-2}$ A m^{-2} is the saturation current. Since I_{ph} is nearly equal to the short-circuit current, we can write the electric power density as[5]

$$P_{\mathrm{el}} = \mathrm{FF}I_{\mathrm{ph}}V_{\mathrm{oc}}. \tag{22}$$

Eqn (15)–(17) and (22) are the key to answering whether room-temperature optical data are suitable for designing high-temperature NF TPV devices.

3 Result and discussion

Fig. 3 presents how the primitive unit cell of tungsten changes during isobaric heating at 0 GPa. Generally, the hotter the lattice, the larger the size. Our full SMM calculations indicate that the atomic volume of tungsten increases significantly from 15.8026 Å^3 at 0 K to 16.3276 Å^3 at 2000 K. This increase is in excellent agreement with the X-ray diffraction measurements of Litasov *et al.*[28] on the equation of state. All relative errors are less than 0.33% in the examined region. This upper limit confirms the accuracy of the Mie–Lennard-Jones potential[36] we have mentioned in Section 2. Note that accurate information about thermal expansion is crucial for ensuring material compatibility and preventing structural damage in multi-component NF TPV

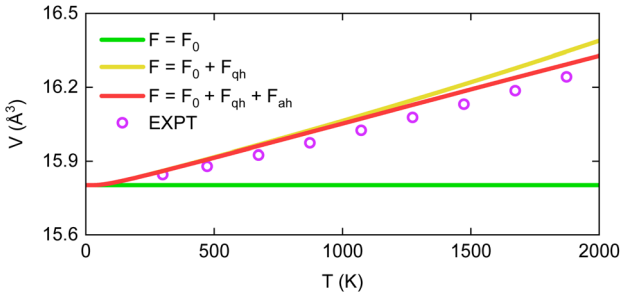

Fig. 3 (Color online) The atomic volume of tungsten as a function of the absolute temperature gained from SMM analyses (solid lines) and X-ray experiments[28] (open symbols).

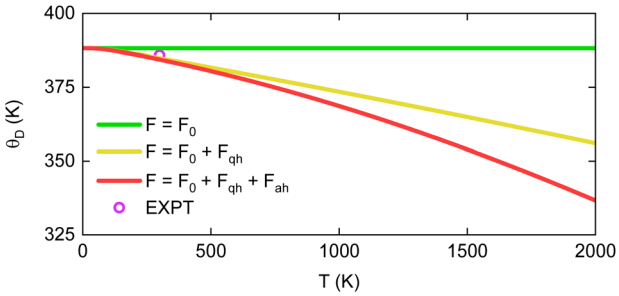

Fig. 5 (Color online) The Debye temperature of tungsten given by SMM approximations (solid lines) and ultrasonic experiments[50] (open symbols).

systems. Therefore, physicists should use modern anharmonic methods to avoid the risk of atomic volume overestimation—a common problem with quasi-harmonic approximations.[47]

Fig. 4 depicts the influence of temperature on the mechanical deformation of tungsten. Overall, there is a considerable drop in elastic moduli along the zero-pressure isobar. Static SMM analyses give us $E = 429.6$ GPa and $G = 166.2$ GPa in the ground state. When the crystal is heated to 2000 K, the above quantities reduce to $E = 358.9$ GPa and $G = 137.7$ GPa in the quasi-harmonic limit. Nonlinear atomic vibrations further lower them to $E = 324.9$ GPa and $G = 122.6$ GPa, consistent with the experimental observations of Lowrie and Gonas[48] ($E = 326.2$ GPa and $G = 125.3$ GPa). This result highlights the role of intrinsic anharmonicity in predicting the elastic behaviors of tungsten at elevated temperatures. If anharmonic contributions are ignored, both axial and shear stiffness will be overestimated. Our conclusion is actively supported by recent theoretical calculations for transition metals under severe conditions.[31,38,49] Thus, the present study would contribute to addressing the strict mechanical requirements of large-scale NF TPV converters.[7]

Fig. 5 shows the Debye temperature of tungsten as a function of the absolute temperature. It is clear to see that θ_D decreases continuously with T. Cold SMM computations yield $\theta_D = 388.2$ K, which is very close to the ultrasonic value of 385.8 K reported by Qi *et al.*[50] After taking into account quasi-harmonic excitations, we observe that θ_D drops almost linearly at an average rate of 0.016 K/K. However, this linearity will be rapidly broken down if we add anharmonic effects to the θ_D–T curve. At $T = 2000$ K, we obtain $\theta_D = 336.7$ K from fully anharmonic SMM analyses. Our theoretical results agree qualitatively well with the entropy-based predictions of Grimvall *et al.*[51] on the nonlinear reduction of θ_D during isobaric heating.

Fig. 6 presents our numerical calculations for the electrical resistivity of tungsten. First, we compare the contributions of different scattering mechanisms [see Fig. 6(a)]. It is possible to divide our studied temperature region into three fundamental

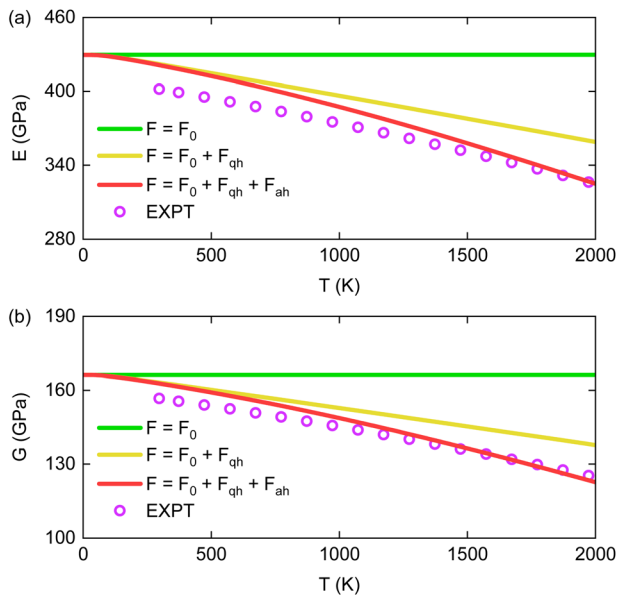

Fig. 4 (Color online) Finite-temperature effects on the Young modulus (a) and the shear modulus (b) of tungsten. Whereas solid lines denote SMM computations, open symbols represent ultrasonic measurements.[48]

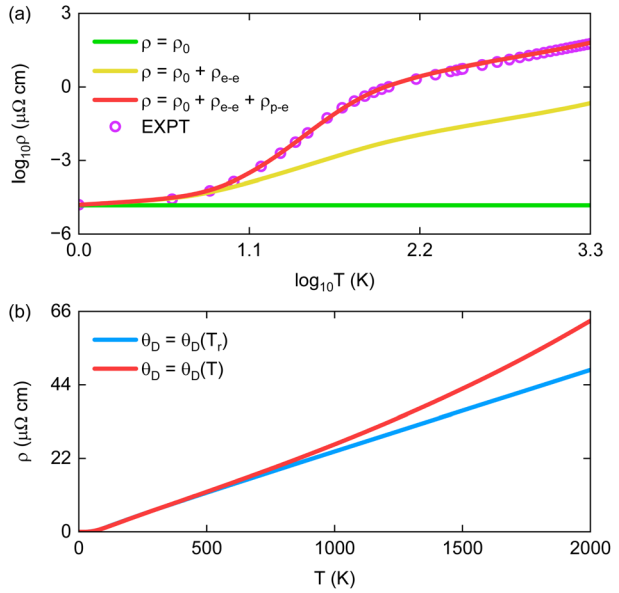

Fig. 6 (Color online) (a) Theoretical (solid lines) and experimental[41] (open symbols) results for the electrical resistivity of tungsten along the ambient isobar. (b) The total resistivity of tungsten derived from the Bloch–Grüneisen law with and without the temperature dependence of the Debye parameter (red line: unfixed θ_D, blue line: fixed θ_D).

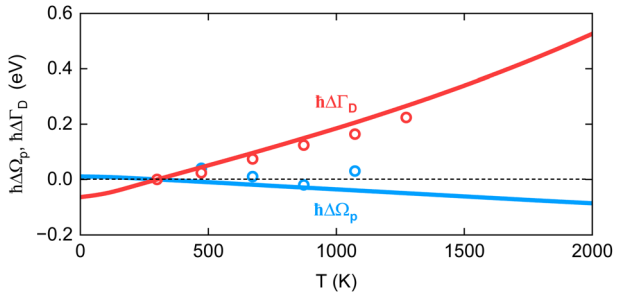

Fig. 7 (Color online) Thermally induced shifts in the plasma and collision frequencies of tungsten. While solid curves are taken from SMM computations, open symbols are extracted from ellipsometry experiments.[17] The dashed horizontal line is added to highlight how the Drude–Lorentz parameters increase/decrease with temperature.

parts: (i) $0 \leq T \leq 4$ K, (ii) $4 \leq T \leq 10$ K, and (iii) $10 \leq T \leq 2000$ K. In part (i), structural defects play a leading role. About 55–100% of the ρ value is attributed to the residual term ρ_0. Going to part (ii), we find that electron–electron interactions get the upper hand. The intrinsic term ρ_{e-e} accounts for 40–60% of the total resistivity. The dominance of phonon-electron scatterings is recorded in part (iii). More than 99% of the specific electrical resistance comes from the vibrational term ρ_{p-e} when the absolute temperature exceeds 60 K. Our results are in good agreement with the experimental data recommended by Desai *et al.*[41] Notwithstanding, we would like to note that eqn (12) may be unsuitable for tungsten at $T \geq 2000$ K because the strong coupling of electronic and atomic vibrations[31] may invalidate the Matthiessen rule.[40]

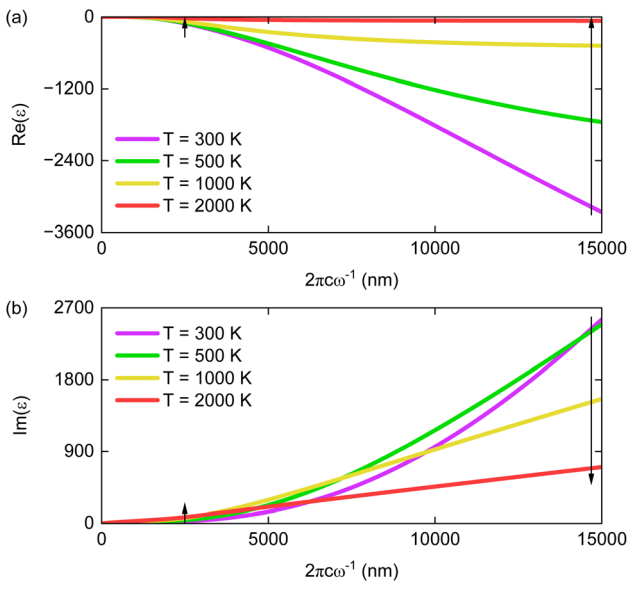

Fig. 8 (Color online) Our theoretical predictions of the real (a) and imaginary (b) dielectric functions of tungsten at different temperatures (colored solid lines). The black arrows are included to elucidate thermal effects in short- and long-wavelength regions. The symbol c stands for the speed of light in a vacuum.

Next, we assess potential risks related to fixing the Debye temperature in eqn (13). It has been frequently assumed that the principal input θ_D of the Bloch–Grüneisen law is thermally insensitive.[52–54] Nevertheless, this assumption does not work in the case of tungsten. Fig. 6(b) shows that the ability to resist electric currents will be strongly underestimated if we rely solely on room-temperature information to conduct SMM analyses. At $T = 2000$ K, the discrepancy between using $\theta_D(T)$ and $\theta_D(T_r)$ is up to 23%. This error can be naturally explained by the quasi-harmonicity and anharmonicity of the bcc lattice (see Fig. 5). Hence, physicists should pay careful attention to the variation of the Debye temperature before investigating the electrical properties of metals and alloys *via* the Bloch–Grüneisen law.[19]

Fig. 7 depicts temperature-induced changes in the Drude–Lorentz parameters of tungsten. Generally, whereas the plasma frequency decreases monotonically during isobaric heating, the collision frequency does the complete opposite. These trends were observed in the *ab initio* simulations of Xu *et al.*[16] At 2000 K, we gain $\hbar\Delta\Omega_p = -0.087$ eV and $\hbar\Delta\Gamma_D = 0.5261$ eV from eqn (15). That means the plasma frequency dwindles by only 1.45% while the collision frequency escalates by up to 822% compared to room-temperature data.[42] In other words, the temperature dependence of the dielectric function primarily stems from the parameter Γ_D. Our physical picture aligns qualitatively with that of Arya *et al.*[17] The gap between theoretical curves and experimental points may be narrowed by considering the impacts of grain size and surface roughness on optical characteristics.

Fig. 8 shows our numerical results for the relative permittivity of tungsten under various thermodynamic conditions. For a specified wavelength, it is conspicuous that the real part $\mathrm{Re}(\varepsilon)$ always grows with temperature [Fig. 8(a)]. Meanwhile, the imaginary part $\mathrm{Im}(\varepsilon)$ behaves quite complexly [Fig. 8(b)]. To clarify the difference, we calculate the first-order derivatives of $\mathrm{Re}(\varepsilon)$ and $\mathrm{Im}(\varepsilon)$ at a given value of the angular frequency by

$$\frac{\mathrm{d}}{\mathrm{d}T}\mathrm{Re}(\varepsilon) \approx \frac{2{\Omega_p}^2\Gamma_D}{\left(\omega^2+{\Gamma_D}^2\right)^2}\frac{\mathrm{d}\Gamma_D}{\mathrm{d}T}, \tag{23}$$

$$\frac{\mathrm{d}}{\mathrm{d}T}\mathrm{Im}(\varepsilon) \approx \frac{{\Omega_p}^2\left(\omega^2-{\Gamma_D}^2\right)}{\omega\left(\omega^2+{\Gamma_D}^2\right)^2}\frac{\mathrm{d}\Gamma_D}{\mathrm{d}T}, \tag{24}$$

where the thermal sensitivity of ε is supposed to depend solely on Γ_D. Since $\mathrm{d}\Gamma_D/\mathrm{d}T$ is never smaller than zero, eqn (23) clearly explains why $\mathrm{Re}(\varepsilon)$ can be viewed as a monotonic increasing function of T. In addition, the appearance of $(\omega^2 - {\Gamma_D}^2)$ in eqn (24) helps us understand positive $\mathrm{Im}(\varepsilon) - T$ correlations in the short-wavelength domain and negative $\mathrm{Im}(\varepsilon) - T$ correlations in the long-wavelength domain. When the difference between ω and Γ_D becomes sufficiently large, we can rewrite eqn (23) and (24) with

$$\frac{\mathrm{d}}{\mathrm{d}T}\mathrm{Re}(\varepsilon) \approx \begin{cases} \dfrac{2{\Omega_p}^2\Gamma_D}{\omega^4}\dfrac{\mathrm{d}\Gamma_D}{\mathrm{d}T}, & \Gamma_D \ll \omega, \\ \dfrac{2{\Omega_p}^2}{{\Gamma_D}^3}\dfrac{\mathrm{d}\Gamma_D}{\mathrm{d}T}, & \Gamma_D \gg \omega, \end{cases} \tag{25}$$

Table 2 The radiative and electric power densities produced by our NF TPV system at various vacuum thicknesses. Whereas the working condition of the tungsten emitter is set to 2000 K, that of the GaSb cell is kept at 300 K

Tungsten dielectric function	d (nm)	P_{rad} (MW m^{-2})	P_{el} (MW m^{-2})
High-temperature Drude–Lorentz model	10000	0.2454	0.0359
	1000	0.2906	0.0439
	100	1.9270	0.2053
	10	7.1655	1.2170
Room-temperature Drude–Lorentz model	10000	0.1405	0.0308
	1000	0.1704	0.0384
	100	0.7591	0.1580
	10	4.0287	1.0869

$$\frac{\mathrm{d}}{\mathrm{d}T}\mathrm{Im}(\varepsilon) \approx \begin{cases} \dfrac{\Omega_p{}^2}{\omega^3}\dfrac{\mathrm{d}\Gamma_D}{\mathrm{d}T}, & \Gamma_D \ll \omega, \\ -\dfrac{\Omega_p{}^2}{\omega\Gamma_D{}^2}\dfrac{\mathrm{d}\Gamma_D}{\mathrm{d}T}, & \Gamma_D \gg \omega. \end{cases} \quad (26)$$

Note that both Re(ε) and Im(ε) vary very rapidly along the ambient isobar. At 15000 nm wavelength, if we heat tungsten from 300 to 2000 K, Re(ε) will undergo a 51-fold growth, and Im(ε) will experience a 3.6-fold reduction. These numbers imply that it is unreasonable to use room-temperature optical databases to model high-temperature NF TPV converters.

Table 2 presents how our NF TPV system generates radiative energy and transforms it into electricity at the emitter temperature of 2000 K. In general, the smaller the vacuum gap, the higher the power density. According to our complete FED computations, once d reaches 10 nm, P_{rad} is up to 7.1655 MW m^{-2}, far beyond the blackbody limit of 0.9068 MW m^{-2}. Likewise, P_{el} climbs significantly by a factor of 34 after switching from the micron regime ($d = 10$ μm) to the nano one ($d = 10$ nm). These dramatic enhancements are due to the quantum tunneling of evanescent waves.[6–8] Our theoretical results reaffirm the enormous potential of NF TPV devices for overcoming energy crises.

Notably, if we omit thermally induced shifts in plasma and collision frequencies as previously done by others,[12–14] we will strongly underestimate both radiative and electric power densities. Take $d = 100$ nm as an example. Applying the room-temperature Drude–Lorentz model gives us $P_{rad} = 0.7591$ MW m^{-2}, which is 2.5 times lower than $P_{rad} = 1.9270$ MW m^{-2} derived from the high-temperature Drude–Lorentz model. A similar situation also occurs for P_{el}, where the deviation between $\varepsilon(T)$- and $\varepsilon(T_r)$-based calculations is up to 23%. Therefore, more efforts are required to expand available optical databases to avoid incorrect conclusions about NF TPV systems. Developing the theoretical scheme in Fig. 1 may be a viable solution to this intriguing problem.

4 Conclusion

With a desire to contribute to the development of NF TPV devices, we have constructed an expeditious analytical approach to predict the physical properties of tungsten in severe environments. This approach has leveraged fundamental equations in solid-state physics to connect different aspects of mechanics, thermodynamics, and electrodynamics. On that basis, we have quantitatively explained how tungsten expands, deforms, resists electric currents, and interacts with electromagnetic waves at elevated temperatures. The roles of quasi-harmonicity, anharmonicity, structural imperfection, electron–electron interaction, and phonon-electron scattering have also been elucidated. Applicable length scales have been discussed in the Appendix. These theoretical insights would be beneficial for controlling the stability, elasticity, emissivity, and compatibility of tungsten in real emitters.

In particular, we have demonstrated that the transformation of heat into electricity in NF TPV converters cannot be properly modeled by using the room-temperature dielectric function alone. The assumption of thermally insensitive Drude–Lorentz parameters has led to the serious underestimation of radiative and electric power densities in our tungsten-GaSb system in both far- and near-field regions. Thus, it is urgently needed to develop high-temperature optical databases to actualize NF TPV applications in the field of energy conversion. Our theoretical scheme may suggest innovative ways to determine optical properties from elastic moduli and equation-of-state parameters, which have been extensively studied under various thermodynamic conditions.

Author contributions

Tran Dinh Cuong: conceptualization, methodology, investigation, writing – original draft, writing – review & editing, visualization. Anh D. Phan: resources, supervision.

Conflicts of interest

The authors declare that they have no known competing financial interests or personal relationships that could have appeared to influence the work reported in this paper.

Data availability

For tungsten, all data supporting our findings are available within the paper. For GaSb, the Python script used to calculate the relative permittivity can be found from the refractiveindex.info-scripts project on GitHub (see https://github.com/polyanskiy/refractiveindex.info-scripts).

Appendix: finite-size effects

In this study, we present theoretical results for bulk tungsten. Meanwhile, the practical thickness of emitter materials in TPV devices can range from nanometers to millimeters.[11,55] Hence, it is interesting to determine: What is the applicable limit of the present theory?

To provide a quick answer to this question, we consider a free-standing tungsten film consisting of N atomic layers in the bcc phase. These atomic layers are divided into 2 surface layers and N–2 internal layers. Since each surface atom loses four nearest neighbors, its ground-state energy (F_0^*) and coupling parameters (k^*, γ_1^*, and γ_2^*) are estimated by

$$F_0^* = \frac{1}{2}F_0,\ k^* = \frac{1}{2}k,\ \gamma_1^* = \frac{1}{2}\gamma_1,\ \gamma_2^* = \frac{1}{2}\gamma_2. \tag{27}$$

Replacing F_0, k, γ_1, and γ_2 in eqn (1), (4) and (6) with F_0^*, k^*, F_0^*, and γ_2^* gives us the surface free energy F^*.[56] For internal atoms, we can use the bulk free energy F to investigate their physical properties. That is because the first coordination number of internal atoms remains unchanged after switching from bulk to nano structures. The above assumptions enable us to derive the average free energy F_{film} per atom from

$$F_{\text{film}} = \frac{2}{N}F^* + \frac{N-2}{N}F. \tag{28}$$

Based on eqn (28), it is feasible to calculate the nearest neighbor distance r_{film} by solving the equation of state at $P = 0$ GPa. Inputting r_{film} into the modified cylindrical method[23] yields the film thickness d_{film} and the Young modulus E_{film} as

$$d_{\text{film}} = (N-1)\frac{r_{\text{film}}}{\sqrt{3}}, \tag{29}$$

$$E_{\text{film}} = \frac{17}{10\pi r_{\text{film}}} \times \left\{ \frac{2}{N}k^*\left[1 + \frac{16{k_{\text{B}}}^2T^2}{k^{*4}}\left(\gamma_1^* + \gamma_2^*\right)^2(X^*+1)(X^*+2)\right]^{-1} + \frac{N-2}{N}k\left[1 + \frac{16{k_{\text{B}}}^2T^2}{k^4}(\gamma_1+\gamma_2)^2(X+1)(X+2)\right]^{-1}\right\}. \tag{30}$$

where X^* is the surface counterpart of X.

Numerical calculations obtained from eqn (29) and (30) are shown in Fig. 9. Overall, there is a growth tendency towards saturation in the $E_{\text{film}} - d_{\text{film}}$ profile. The elastic properties of macro- and nano-structured systems will become hard to distinguish if the film thickness exceeds 300 nm. This number suggests that the theoretical results presented in the main text should only be applied to tungsten emitters greater than 300 nm in size. Our recommendation agrees well with recent electron transport measurements,[57] in which the electrical anisotropy of tungsten films vanishes at $d_{\text{film}} = 320$ nm.

To capture the optical behaviors of tungsten at $d_{\text{film}} < 300$ nm, we need to add the effects of grain boundaries to the SMM model. It has been demonstrated that the thinner the film, the smaller the grain size. This phenomenon strongly enhances the contribution

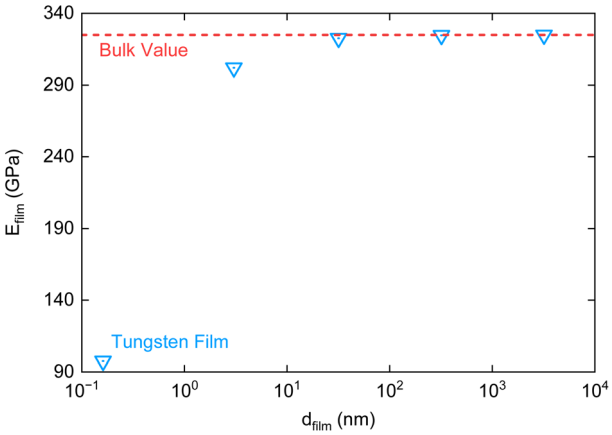

Fig. 9 (Color online) The Young modulus of tungsten as a function of film thickness obtained from SMM calculations at 2000 K.

of electron-grain scatterings to the collision frequency.[17] However, modeling grain boundaries and their interactions with electrons is a challenging problem. Additionally, the A15 phase may appear in the sub-300 nm region.[58] Since the A15 structure has a much higher electrical resistivity than the bcc structure,[59] the appearance of A15 atoms may significantly alter the optical properties of tungsten at the nanoscale. Nevertheless, the A15-bcc transition is very complex because it depends on various factors, including impurities, substrates, pressures, and temperatures. Therefore, the intriguing problems above deserve consideration in separate theoretical works in the future.

References

1 Z. Omair, G. Scranton, L. M. Pazos-Outón, T. P. Xiao, M. A. Steiner, V. Ganapati, P. F. Peterson, J. Holzrichter, H. Atwater and E. Yablonovitch, Ultraefficient thermophotovoltaic power conversion by band-edge spectral filtering, *Proc. Natl. Acad. Sci. U. S. A.*, 2019, **116**, 15356.
2 D. Fan, T. Burger, S. McSherry, B. Lee, A. Lenert and S. R. Forrest, Near-perfect photon utilization in an air-bridge thermophotovoltaic cell, *Nature*, 2020, **586**, 237.
3 T. Burger, C. Sempere, B. Roy-Layinde and A. Lenert, Present efficiencies and future opportunities in thermophotovoltaics, *Joule*, 2020, **4**, 1660.
4 A. LaPotin, K. L. Schulte, M. A. Steiner, K. Buznitsky, C. C. Kelsall, D. J. Friedman, E. J. Tervo, R. M. France, M. R. Young, A. Rohskopf, S. Verma, E. N. Wang and A. Henry, Thermophotovoltaic efficiency of 40%, *Nature*, 2022, **604**, 287.
5 M. Laroche, R. Carminati and J. J. Greffet, Near-field thermophotovoltaic energy conversion, *J. Appl. Phys.*, 2006, **100**, 063704.
6 J. Song, J. Han, M. Choi and B. J. Lee, Modeling and experiments of near-field thermophotovoltaic conversion: A review, *Sol. Energy Mater. Sol. Cells*, 2022, **238**, 111556.
7 R. Mittapally, A. Majumder, P. Reddy and E. Meyhofer, Near-field thermophotovoltaic energy conversion: Progress and opportunities, *Phys. Rev. Appl.*, 2023, **19**, 037002.

8 S. A. Biehs, R. Messina, P. S. Venkataram, A. W. Rodriguez, J. C. Cuevas and P. Ben-Abdallah, Near-field radiative heat transfer in many-body systems, *Rev. Mod. Phys.*, 2021, **93**, 025009.

9 K. Park, S. Basu, W. P. King and Z. M. Zhang, Performance analysis of near-field thermophotovoltaic devices considering absorption distribution, *J. Quant. Spectrosc. Radiat. Transfer*, 2008, **109**, 305.

10 K. Chen, P. Santhanam and S. Fan, Suppressing sub-bandgap phonon-polariton heat transfer in near-field thermophotovoltaic devices for waste heat recovery, *Appl. Phys. Lett.*, 2015, **107**, 091106.

11 G. R. Bhatt, B. Zhao, S. Roberts, I. Datta, A. Mohanty, T. Lin, J. M. Hartmann, R. St-Gelais, S. Fan and M. Lipson, Integrated near-field thermo-photovoltaics for heat recycling, *Nat. Commun.*, 2020, **11**, 2545.

12 J. Y. Chang, Y. Yang and L. Wang, Tungsten nanowire based hyperbolic metamaterial emitters for near-field thermophotovoltaic applications, *Int. J. Heat Mass Transfer*, 2015, **87**, 237.

13 J. I. Watjen, X. L. Liu, B. Zhao and Z. M. Zhang, A computational simulation of using tungsten gratings in near-field thermophotovoltaic devices, *J. Heat Transfer*, 2017, **139**, 052704.

14 T. Wang, S. Li and J. Zhao, Selectively enhanced near-field radiative transfer between tungsten and GaSb with Si nano square gratings for thermophotovoltaics, *Sol. Energy Mater. Sol. Cells*, 2025, **289**, 113670.

15 M. Minissale, C. Pardanaud, R. Bisson and L. Gallais, The temperature dependence of optical properties of tungsten in the visible and near-infrared domains: An experimental and theoretical study, *J. Phys. D: Appl. Phys.*, 2017, **50**, 455601.

16 M. Xu, J. Y. Yang and L. Liu, Temperature-dependent dielectric functions of bcc transition metals Cr, Mo, and W from ultraviolet to infrared regions: A theoretical and experimental study, *J. Appl. Phys.*, 2018, **123**, 155102.

17 M. Arya, A. Ganguly, G. V. Krishnamurthy, S. S. Rout, L. Gurevich, T. Krekeler, M. Ritter, K. Pedersen, M. Störmer, A. Y. Petrov, M. Eich and M. Chirumamilla, Which factor determines the optical losses in refractory tungsten thin films at high temperatures?, *Appl. Surf. Sci.*, 2022, **588**, 152927.

18 O. L. Anderson, A simplified method for calculating the Debye temperature from elastic constants, *J. Phys. Chem. Solids*, 1963, **24**, 909.

19 A. Jayakumar, V. Dixit, S. Jose, V. B. Kamble and D. Jaiswal-Nagar, Charge transport variation from Bloch–Grüneisen to Mott variable range hopping and transport change due to hydrogenation in Palladium thin films, *Sci. Rep.*, 2021, **11**, 22298.

20 J. D. Jackson, *Classical Electrodynamics*, Wiley, New York, 1999.

21 K. Masuda-Jindo, V. V. Hung and P. D. Tam, Thermodynamic quantities of metals investigated by an analytic statistical moment method, *Phys. Rev. B*, 2003, **67**, 094301.

22 T. D. Cuong and A. D. Phan, Novel insights into vacancy effects on high-pressure melting of W from anharmonic statistical moment method, *Int. J. Refract. Met. Hard Mater.*, 2025, **127**, 106962.

23 T. D. Cuong and A. D. Phan, Theoretical investigation into melt and shock behaviors of tantalum under extremes, *Physica B*, 2025, **717**, 417767.

24 D. Polder and M. Van Hove, Theory of radiative heat transfer between closely spaced bodies, *Phys. Rev. B*, 1971, **4**, 3303.

25 Y. Liu, Y. Yuan, X. Chen, J. Peng, Z. Li, J. Ge, X. Lv, J. Li, H. Wang, L. Tang, J. Shao, X. Chai, Y. Zhang, X. Zeng and X. Gao, Experimental and simulation investigations on the impact of non-uniform GaSb cells temperature in thermophotovoltaic systems, *J. Appl. Phys.*, 2025, **138**, 105704.

26 Y. Ding, T. Fang, S. Jiang, Y. Zhang, X. Huang and T. Cui, Unified equation of state of tungsten up to 527 GPa using modified toroidal diamond anvil cells, *Phys. Rev. B*, 2025, **111**, 214101.

27 Z. M. Zhang, *Nano/Microscale Heat Transfer*, McGraw-Hill, New York, 2007.

28 K. D. Litasov, P. N. Gavryushkin, P. I. Dorogokupets, I. S. Sharygin, A. Shatskiy, Y. Fei, S. V. Rashchenko, Y. V. Seryotkin, Y. Higo, K. Funakoshi and E. Ohtani, Thermal equation of state to 33.5 GPa and 1673 K and thermodynamic properties of tungsten, *J. Appl. Phys.*, 2013, **113**, 133505.

29 P. I. Dorogokupets, A. M. Dymshits, K. D. Litasov and T. S. Sokolova, Thermodynamics and equations of state of iron to 350 GPa and 6000 K, *Sci. Rep.*, 2017, **7**, 41863.

30 National Academies of Sciences, Engineering, and Medicine, *Fundamental Research in High Energy Density Science*, The National Academies Press, Washington, DC, 2023.

31 A. Forslund, J. H. Jung, P. Srinivasan and B. Grabowski, Thermodynamic properties on the homologous temperature scale from direct upsampling: Understanding electron-vibration coupling and thermal vacancies in bcc refractory metals, *Phys. Rev. B*, 2023, **107**, 174309.

32 X. Zhang, S. V. Divinski and B. Grabowski, Ab initio machine-learning unveils strong anharmonicity in non-Arrhenius self-diffusion of tungsten, *Nat. Commun.*, 2025, **16**, 394.

33 V. V. Hung and N. T. Hai, Investigation of the elastic moduli of face and body-centered cubic crystals, *Comput. Mater. Sci.*, 1999, **14**, 261.

34 H. K. Hieu, Systematic prediction of high-pressure melting curves of transition metals, *J. Appl. Phys.*, 2014, **116**, 163505.

35 V. V. Hung, D. T. Hai and H. K. Hieu, Thermodynamic properties and structural phase transition of cerium under high pressure, *Vacuum*, 2015, **114**, 119.

36 M. N. Magomedov, The calculation of the parameters of the Mie-Lennard-Jones potential, *High Temp.*, 2006, **44**, 513.

37 G. Leibfried and W. Ludwig, Theory of anharmonic effects in crystals, *Solid State Phys.*, 1961, **12**, 275.

38 T. D. Cuong and A. D. Phan, Modeling the elastic properties of bcc iron in Earth's core by quantum statistical physics, *Vacuum*, 2025, **237**, 114116.

39 Y. Liang, Z. Fu, X. Yuan, S. Wang, Z. Zhong and W. Zhang, An unexpected softening from WB_3 to WB_4, *Europhys. Lett.*, 2012, **98**, 66004.
40 P. L. Rositter, *The Electrical Resistivity of Metals and Alloys*, Cambridge University Press, Cambridge, 1991.
41 P. D. Desai, T. K. Chu, H. M. James and C. Y. Ho, Electrical resistivity of selected elements, *J. Phys. Chem. Ref. Data*, 1984, **13**, 1069.
42 A. D. Rakić, A. B. Djurišić, J. M. Elazar and M. L. Majewski, Optical properties of metallic films for vertical-cavity optoelectronic devices, *Appl. Opt.*, 1998, **37**, 5271.
43 S. Adachi, Optical dispersion relations for GaP, GaAs, GaSb, InP, InAs, InSb, $Al_xGa_{1-x}As$, and $In_{1-x}Ga_xAs_yP_{1-y}$, *J. Appl. Phys.*, 1989, **66**, 6030.
44 M. N. Polyanskiy, Refractiveindex.info database of optical constants, *Sci. Data*, 2024, **11**, 94.
45 R. Kubo, The fluctuation-dissipation theorem, *Rep. Prog.*, 1966, **29**, 255.
46 W. Eckhardt, Macroscopic theory of electromagnetic fluctuations and stationary radiative heat transfer, *Phys. Rev. A*, 1984, **29**, 1991.
47 E. J. Blancas, A. Lobato, F. Izquierdo-Ruiz, A. M. Márquez, J. M. Recio, P. Nath, J. J. Plata and A. Otero-de-la-Roza, Thermodynamics of solids including anharmonicity through quasiparticle theory, *npj Comput. Mater.*, 2024, **10**, 267.
48 R. Lowrie and A. M. Gonas, Dynamic elastic properties of polycrystalline tungsten, 24^o to 1800^oC, *J. Appl. Phys.*, 1965, **36**, 2189.
49 T. D. Cuong and A. D. Phan, Calculation of the melting curve, shock Hugoniot, and ramp adiabat of nickel up to the super-Earth pressure–temperature range, *J. Appl. Phys.*, 2025, **137**, 125902.
50 X. Qi, N. Cai, T. Chen, S. Wang and B. Li, Experimental and theoretical studies on the elasticity of tungsten to 13 GPa, *J. Appl. Phys.*, 2018, **124**, 075902.
51 G. Grimvall, M. Thiessen and A. F. Guillermet, Thermodynamic properties of tungsten, *Phys. Rev. B*, 1987, **36**, 7816.
52 N. Q. Hoc, B. D. Tinh and N. D. Hien, Influence of temperature and pressure on the electrical resistivity of gold and copper up to 1350 K and 100 GPa, *Mater. Res. Bull.*, 1987, **128**, 110874.
53 A. Bid, A. Bora and A. K. Raychaudhuri, Temperature dependence of the resistance of metallic nanowires of diameter >15nm: Applicability of Bloch-Grüneisen theorem, *Phys. Rev. B:Condens. Matter Mater. Phys.*, 2006, **74**, 035426.
54 K. Ohta, Y. Kuwayama, K. Hirose, K. Shimizu and Y. Ohishi, Experimental determination of the electrical resistivity of iron at Earth's core conditions, *Nature*, 2016, **534**, 95.
55 C. S. Prasad and G. V. Naik, Non-Hermitian selective thermal emitter for thermophotovoltaics, *npj Nanophoton.*, 2024, **1**, 44.
56 D. D. Phuong, N. T. Hoa, V. V. Hung, D. Q. Khoa and H. K. Hieu, Mechanical properties of metallic thin films: Theoretical approach, *Eur. Phys. J. B*, 2016, **89**, 84.
57 P. Zheng and D. Gall, The anisotropic size effect of the electrical resistivity of metal thin films: Tungsten, *J. Appl. Phys.*, 2017, **122**, 135301.
58 A. Chattaraj, J. Asirvatham, G. Das, G. Manna, P. Saha, V. Kumar and A. Kanjilal, Growth-dependent structural ordering and stability in β-tungsten films for spintronic applications, *J. Appl. Phys.*, 2022, **131**, 125301.
59 Y. J. Kim, S. G. Kang, Y. Oh, G. W. Kim, I. H. Cha, H. N. Han and Y. K. Kim, Microstructural evolution and electrical resistivity of nanocrystalline W thin films grown by sputtering, *Mater. Charact.*, 2018, **145**, 473.